

Valence Photoionization and Energetics of Vanillin, a Sustainable Feedstock Candidate

Published as part of *The Journal of Physical Chemistry virtual special issue "Cheuk-Yiu Ng Festschrift"*.

Xiangkun Wu, Xiaoguo Zhou,* Saša Bjelić, Patrick Hemberger, and Andras Bodi*

 Cite This: *J. Phys. Chem. A* 2021, 125, 3327–3340

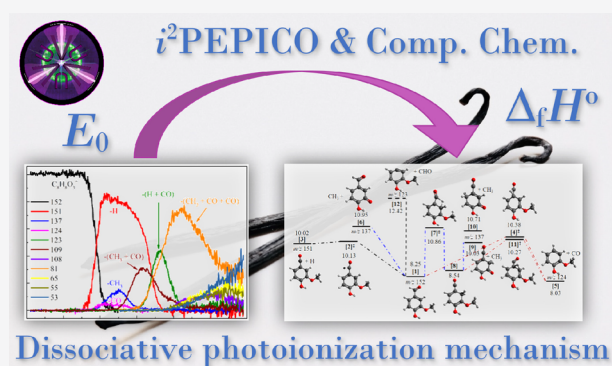
 Read Online

ACCESS |

 Metrics & More

 Article Recommendations

ABSTRACT: We studied the valence photoionization of vanillin by photoelectron photoion coincidence spectroscopy in the 8.20–19.80 eV photon energy range. Vertical ionization energies by EOM-IP-CCSD calculations reproduce the photoelectron spectral features. Composite method calculations and Franck–Condon simulation of the weak, ground-state band yield the adiabatic ionization energy of the most stable vanillin conformer as 8.306(20) eV. The lowest energy dissociative photoionization channels correspond to hydrogen atom, carbon monoxide, and methyl losses, which form the dominant $C_8H_7O_3^+$ (m/z 151) and the less intense $C_7H_8O_2^+$ (m/z 124) and $C_7H_5O_3^+$ (m/z 137) fragment ions in parallel dissociation channels at modeled 0 K appearance energies of 10.13(1), 10.40(3), and 10.58(10) eV, respectively. On the basis of the breakdown diagram, we explore the energetics of sequential methyl and carbon monoxide loss channels, which dominate the fragmentation mechanism at higher photon energies. The 0 K appearance energy for sequential CO loss from the m/z 151 fragment to $C_7H_7O_2^+$ (m/z 123) is 12.99(10) eV, and for sequential CH_3 loss from the m/z 123 fragment to $C_6H_4O_2^+$ (m/z 108), it is 15.40(20) eV based on the model. Finally, we review the thermochemistry of the bi- and trifunctionalized benzene derivatives guaiacol, hydroxybenzaldehyde, anisaldehyde, and vanillin. On the basis of isodesmic functional group exchange reactions, we propose new enthalpies of formations, among them $\Delta_f H^\circ_{298K}(\text{vanillin, g}) = -383.5 \pm 2.9 \text{ kJ mol}^{-1}$. These mechanistic insights and ab initio thermochemistry results will support analytical works to study lignin conversion involving vanillin.



1. INTRODUCTION

Vanillin (4-hydroxy-3-methoxybenzaldehyde, $C_8H_8O_3$, 152 g mol^{-1}), a phenolic ether containing methoxy, hydroxy, and aldehyde functional groups, is one of the rare biomass-based aromatic compounds extracted on an industrial scale.¹ Vanillin is also a widely used and important flavoring and fragrance ingredient with global demand of ~ 20 000 tons per year.² It is active in biological systems as a free radical scavenger.³

With the shale gas revolution, the availability of non-renewable aromatic feedstocks has shrunk,⁴ which makes lignin valorization to yield phenolics more attractive.^{5,6} Vanillin, in particular, gained attention as a base for renewable polymers.⁷ Lignin depolymerization strategies exist from unaltered protolignin that yield monomers with close to theoretical yields.^{8–10} However, of the vast amount of 150 billion tons of lignin synthesized by plants each year, only ~ 50 million tons are commercially available, 40 million tons of which is extracted in Kraft pulping, i.e., paper making.¹¹ Pulping increases the density of the strong carbon–carbon bonds at the expense of β -O-4 ether bonds in lignin. Kraft lignin, a cross-linked, three-dimensional biopolymer of aromatic build-

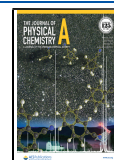
ing blocks, is best described as a supramolecular self-assembled chaos¹² with recalcitrant, interaromatic C–C bonds. Only a fraction is subjected to valorization pathways, such as catalytic fast pyrolysis,^{13,14} oxidative biphasic depolymerization,¹⁵ or high-temperature electrolysis,¹⁶ and most of it is only thermally exploited. Although oxidative lignin depolymerization has been studied for a long time, questions still abound regarding the detailed mechanism.^{17,18}

Among synchrotron vacuum ultraviolet photoionization techniques for probing chemistry,¹⁹ imaging photoelectron photoion coincidence spectroscopy (iPEPICO) has been proven to be a valuable analytical tool to unveil the pyrolysis mechanism of lignin model compounds.^{20–22} Isomer-selective

Received: January 30, 2021

Revised: March 21, 2021

Published: April 19, 2021



PEPICO detection relies on the photoion mass-selected threshold photoelectron spectrum (ms-TPES), i.e., the photoelectron spectrum belonging to a single ion m/z channel, recorded in a multiplexed way.²³ Besides the Franck–Condon modeling of ms-TPES,²⁴ this approach profits greatly from the availability of reference spectra, as was shown for fulvenone ketene,²⁵ a central reactive intermediate in guaiacol catalytic fast pyrolysis.²² Furthermore, although ion velocity map imaging can help distinguish between fragmentationless photoionization of neutrals emanating directly from a reactor and scattered species or dissociative photoionization of heavier neutrals leading to the same m/z peak,²⁶ the assignment is greatly facilitated by known reference breakdown diagrams. Cations of similar size as vanillin, e.g., adipic acid²⁷ or thymine,²⁸ can exhibit a varied and quickly changing fragmentation pattern as a function of internal energy, which is difficult to predict theoretically.

Therefore, the detailed investigation of vanillin valence photoionization is desirable to lay the groundwork for studies on the oxidative depolymerization of lignin and, in particular, vanillin oxidation to vanillic acid.²⁹ Although vanillin is an everyday compound, its valence photoionization has seldom been investigated. Takahashi et al. studied the VUV mass spectrometry of coniferyl and sinapyl alcohols and reported data on vanillin as a potential contaminant.³⁰ They reported a vanillin ionization energy of 8.30 ± 0.05 eV based on thermal desorption molecular beam photoionization mass spectrometry, confirming an earlier value,³¹ and also proposed the m/z 151 peak to be due to dissociative ionization of vanillin. Shu et al. vaporized a vanillin aerosol at 400 K and reported its fragmentation-free photoionization mass spectrum using a Kr/He VUV lamp with the main emission at 10.03 eV.³² Betancourt et al. studied vanillin valence photoionization most in detail by recording the partial ion yield (photoionization) spectrum of vanillin from 12 to 21 eV and reported observed and computed fragment ion appearance potentials.³³ At 12 eV photon energy, they only saw the parent ion in the mass spectrum. As we will show later, the vanillin ion almost completely disappears from our breakdown diagram at this energy. It dissociates predominantly by H and, to a limited degree, by CH_3 and CO loss. Despite the apparent contradiction, both sets of experimental results are probably correct: the vanillin parent ion is metastable, and the appearance of the fragment ions is blue-shifted by the kinetic shift.³⁴ The magnitude of the kinetic shift depends on the time scale of the experiment. In the absence of experimental rate information and a statistical model,³⁵ the rise of a fragment ion signal in the photoionization spectrum cannot be simply correlated to the dissociative photoionization (DPI) threshold. Betancourt et al. also calculated the DPI free energy for H loss as 11.93 eV and proposed a number of bond-breaking dissociation processes. The fragmentation mechanism of all but the smallest organic cations often involves isomerization steps,^{36–39} which requires a statistical model to account for kinetic and competitive shifts³⁵ to reveal the dissociative photoionization mechanism and energetics.

In addition to being an analytical tool,²⁶ PEPICO with tunable vacuum ultraviolet (VUV) synchrotron radiation is the method of choice to reveal dissociative photoionization mechanisms and energetics.^{40,41} By tuning the photon energy and analyzing the electron kinetic energy, the internal energy deposited in the parent ion and, thus, the internal energy available for fragmentation are controlled. The fractional

abundance of the parent and fragment ions in threshold ionization is plotted in the breakdown diagram as a function of photon energy. If the parent ion is metastable close to the dissociative photoionization threshold and the acceleration region is long in the mass spectrometer, slow dissociation rate constants in the 10^3 – 10^7 s⁻¹ range result in asymmetrical fragment ion peak shapes and can be extracted based on the ion optics parameters.⁴² PEPICO unveiled complex dissociation mechanisms with parallel and sequential steps⁴³ and delivered accurate thermochemistry and energetics of elusive species.^{44–46} It can even support ab initio simulations of mass spectra.^{28,47}

This work will use photoelectron photoion coincidence spectroscopy to record and model the breakdown diagram of vanillin taking kinetic and competitive shifts explicitly into account in a statistical framework.³⁵ Quantum chemical calculations and the statistical model of dissociative photoionization reveal the fragmentation mechanism and energetics. The results are relevant when probing vanillin synthesis and decomposition utilizing photoionization techniques. Since the dissociative photoionization model does not yield new thermochemical values directly, we will address the thermochemistry of multiply functionalized benzene derivatives computationally by isodesmic reaction energy calculations relying on the known, monofunctionalized species, using various composite methods. Besides confirming the accuracy of the reaction energies for analogous reactions and deriving new values for the guaiacol, anisaldehyde, and hydroxybenzaldehyde enthalpies of formation, we will also obtain a new value for the vanillin enthalpy of formation.

2. EXPERIMENTAL AND COMPUTATIONAL

Experiments were performed at the VUV beamline of the Swiss Light Source, Paul Scherrer Institute. The reader is referred to previous publications for the details of the beamline and the double imaging photoelectron photoion coincidence (CRF-PEPICO) spectrometer.^{48,49} Synchrotron radiation, generated by a bending magnet, was collimated, dispersed by a grazing incidence monochromator with a 600 lines-mm⁻¹ laminar grating, and focused at a 200 μm exit slit in a differentially pumped rare gas filter with a 2–8 meV resolution depending on the photon energy. The filter was filled with a mixture of neon and argon, or pure neon at a pressure of 10 mbar over an optical length of 10 cm to suppress higher-order radiation above 15.5 and 21.5 eV, respectively. The photon energy was calibrated using the Ar 11s'–13s' autoionization lines in first and second orders of the grating.⁵⁰ The photon beam entered the experimental chamber with the ionization region ~ 50 cm downstream from the focus. Photoionization data were obtained with an average step size of 12 meV below 14 eV and 25 meV below 19.8 eV using an integration time of 60–180 s. The breakdown diagram energy range of H loss was also recorded using a lower extraction field with a step size of 15 meV and an integration time of 180 s.

The vapor pressure of vanillin (Sigma-Aldrich, 99%) was found to be too low to use an external effusive sample inlet. However, when the sample was placed directly in a small beaker in a DN200 cross attached to the ionization chamber, the vapor pressure was sufficient to run the measurement at room temperature.

The photon beam ionizes the sample vapor in the experimental chamber, and electrons and ions produced in the ionization volume are extracted in opposite directions by a

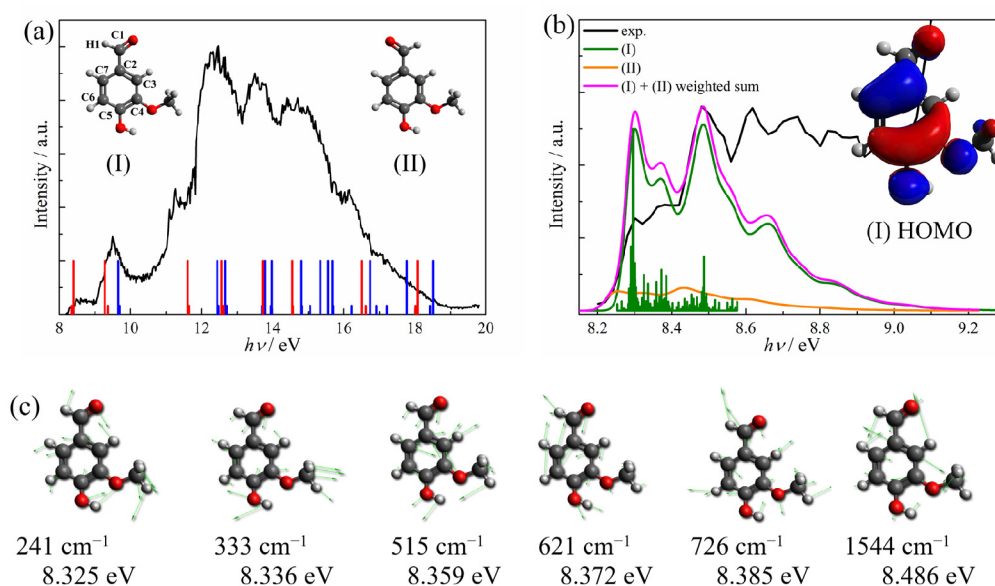


Figure 1. (a) Threshold photoelectron spectrum of vanillin in the photon energy range of 8.20–19.80 eV. The diminishing signal above 16 eV is due to dropping VUV flux. Tall and short sticks show the vertical ionization energies calculated at the EOM-IP-CCSD/cc-pVTZ level for conformers I and II, respectively. Red and blue sticks indicate A'' and A' states, respectively. (b) Franck–Condon model of the ground cation state plotted against the experimental spectrum in the 8.2–9.2 eV energy range shown together with the line spectrum (dark green) and the HOMO of conformer I. (c) Six of the most intense vibrational modes contributing to the spectrum of I in (b), together with the vibrational frequencies and the energy of the transition in the spectrum.

216 or 108 $\text{V}\cdot\text{cm}^{-1}$ constant electric field. After reaching their final energy and passing a flight tube, both are detected by position-sensitive delay-line anode detectors (Roentdek, DLD40). Electrons were detected in velocity map imaging conditions to measure their kinetic energy, whereas space focusing conditions were applied on the ion side. As the electron time-of-flight (TOF) is negligible relative to the ion TOF, electron hits can be used as the start signal for the ion TOF analysis.⁵¹ Threshold electrons with less than 2 meV kinetic energy and kinetic electrons without an off-axis momentum component are projected together onto the central spot of the detector. In order to obtain the threshold ionization signal, the hot electron contamination of the center signal was subtracted based on the signal in a small ring around the center spot as proposed by Sztáray and Baer.⁵² Threshold ionization mass spectra are used to plot the breakdown diagram by evaluating the parent and daughter ion fractional abundances as a function of photon energy. To maintain high electron kinetic energy resolution and ensure a long ion residence time in the acceleration region for the analysis of metastable dissociations, a relatively low extraction field is used. Combined with the large, ~ 2 mm spot size, the thermal and instrumental peak widths at room temperature do not allow for baseline separation of the m/z 152 and 151 peaks, i.e., that of the parent ion and the H-loss fragment. In order to determine their fractional abundances, a center-of-gravity (CoG) deconvolution approach was used.^{53–55} The CoG of the band encompassing the two peaks is determined by

$$\mu = \frac{\int t \cdot \text{TOF}(t) dt}{\int \text{TOF}(t) dt} \quad (1)$$

where μ is the band CoG based on the time-of-flight distribution, $\text{TOF}(t)$. The fractional abundance of each peak can then be found by

$$\mu = at_1 + (1 - a)t_2 \quad (2)$$

where t_1 and t_2 are the peak centers and a , $1 \geq a \geq 0$, is the fractional abundance of the first ion.

The statistical modeling approach to dissociative photoionization was described elsewhere,³⁵ and only key aspects are emphasized here. When the internal energy of parent ions is lower than the dissociation energy, no fragment ions appear, and the parent abundance is 100%. As the photon energy is increased, the fractional abundance of the parent ion begins to decrease and that of the fragment ions starts to increase. In fast dissociations without competing channels, the integral of the internal energy distribution above the barrier yields the abundance of the fragment ion. If the parent ion is metastable or if fragmentation processes compete, the density of states of the parent ion and the number of states of the transition state(s) are used to calculate the unimolecular dissociation rate constant, according to RRKM theory as^{56–58}

$$k(E) = \frac{\sigma \cdot N^\ddagger(E - E_0)}{h \cdot \rho(E)} \quad (3)$$

where σ corresponds to the symmetry of the reaction coordinate, $N^\ddagger(E - E_0)$ is the number of states of the transition state at the excess energy, $E - E_0$, E_0 is the 0 K appearance energy, h is Planck's constant, and $\rho(E)$ is the density of states of the precursor. The appearance energy is an adjustable parameter, and the frequencies of the transitional modes in the transition state are scaled by a common, fitted factor to reproduce the observed breakdown diagram and the absolute or relative rate constants. The internal energy distribution of the fragment ion, available in sequential dissociation processes, is obtained by partitioning the excess energy statistically between the fragment ion, the leaving neutral, and the newly formed rotational and translational degrees of freedom without adjustable parameters. The

uncertainty of the fitted 0 K appearance energies has been determined by changing the appearance energy and optimizing the remaining parameters in the model until the resulting fit failed to reproduce the experimental data. The statistical partitioning of the excess energy is only applicable in the absence of a reverse barrier. An energetic, tight transition state often entails a repulsive dissociation coordinate with supra-statistical kinetic energy release.²⁸ Aside from H loss, which exhibits a small reverse barrier (see below), we have not included sequential processes in the model after a tight transition state with a substantial reverse barrier.

Computed vibrational frequencies, rotational constants, and appearance energies are used to construct the initial statistical model. To provide this input, the neutral, the parent ion, the fragmentation products, intermediates, and transition states were located on the ground state potential energy surface using density functional theory at the B3LYP/6-311++G(d,p) level. The energies of the stationary points were further refined using Gaussian-4 (G4) theory⁵⁹ as implemented in the Gaussian 16 A.03 program package.⁶⁰ The CBS-QB3 and CBS-APNO composite methods⁶¹ were also used to confirm the vanillin ionization energy. Together with the W1 method,⁶² they were applied to compute isodesmic reaction energies and obtain new enthalpies of formation for bifunctionalized benzene derivatives and vanillin. In addition, equation of motion ionization potential coupled cluster calculations⁶³ were carried at the EOM-IP-CCSD/cc-pVTZ level of theory using Q-Chem 4.3 to obtain vertical ionization energies to the vanillin cation ground and excited electronic states.⁶⁴

3. RESULTS AND DISCUSSION

3.1. Threshold Photoelectron Spectrum. Figure 1a shows the TPES of vanillin recorded in the 8.20–19.80 eV photon energy range. The bond energy of the OH...O(CH₃) intramolecular hydrogen bond in vanillin is ~20 kJ mol⁻¹, which means that any vanillin conformer without this bond will have negligible abundance at room temperature. This leaves us with two low-energy conformers of C_s symmetry with non-negligible population, differing only in the orientation of the aldehyde group. Conformer I is more stable than conformer II by 4.8 kJ mol⁻¹ at the G4 level of theory (see insets in Figure 1a). At room temperature, the population of II is, thus, ~12%, and the photoelectron spectrum is mainly determined by conformer I. Vertical ionization energies of the neutral were calculated at the EOM-IP-CCSD/cc-pVTZ level and can be compared with the TPES bands. The distribution of the A'' and A' states of II mirrors that of I below 15 eV (Figure 1), and significant differences are only seen in the A' states at around 16 eV. This means that the outer valence structures of the two conformers are very much alike, in contrast with substituted cyclohexanes, in which conformational change was associated with little energy change but large outer valence structural changes.³⁹ Furthermore, the TPES band structure lines up quite well with the computed cation electronic state levels, which gives us confidence in the EOM-IP-CCSD calculations. This good agreement implies that the weak band starting at ~8.2 eV is not a particularly intense hot band but indeed the ground state band of the photoelectron spectrum. Some structure is seen in the spectrum around 12.5 eV, which could be due to either a vibrational progression or strong origin transitions to three excited cation states in this energy region.

The ground-state band, plotted in detail in Figure 1b, exhibits some structure. Due to the poor resolution and signal-to-noise ratio, its physical meaning is ambiguous. In this case, the adiabatic ionization energy cannot be determined without a Franck–Condon analysis of the spectrum as the origin transition cannot be identified clearly.⁶⁵ Therefore, we carried out a Franck–Condon simulation of the ground-state photoelectron spectrum of the two conformers at the B3LYP/6-311++G(d,p) level of theory in the double harmonic approximation, convoluted the line spectra with a 45 meV full width at half-maximum Gaussian to account for the rotational envelope, and weighted the results with the computed room temperature conformer abundances. Hundreds of vibrational transitions make up the spectrum, but the most active transitions correspond to the origin transition, ring deformation modes, and in-plane bending (scissoring) modes of the functional groups. The most intense standalone transitions correspond to pure excitation of a single vibrational mode, six of which are shown in Figure 1c. As seen in the line spectrum, the largest Franck–Condon factor among these is computed for the ring deformation mode at 1544 cm⁻¹, which can be explained by the geometry change upon ionization. The highest occupied molecular orbital (HOMO, Figure 1b) has an antibonding character along the C2–C3, C6–C7, as well as the C5–O and C4–O bonds. Accordingly, the bond lengths decrease by 0.02, 0.02, 0.04, and 0.05 Å, respectively, upon ionization to the ground electronic cation state, while the C2–C7 bond, where the vanillin HOMO has a bonding character, increases in length by 0.04 Å. While the simulated ground-state spectrum falls off quite quickly with increasing energy, the experimental spectrum levels off before the onset of the next, excited-state band, centered at ~9.5 eV. Similar to the TPES of dimethyl carbonate, this may be due to excitations to the Rydberg manifold belonging to the first excited state, followed by autoionization to the ground state.³⁶ Three simulated peaks can be tentatively aligned with apparent peaks in the experimental spectrum by shifting the ionization energy of I to 8.295(10) eV. Taking into account the 11 meV Stark shift due to the constant 216 V·cm⁻¹ extraction field,⁶⁶ this yields a vanillin I adiabatic ionization energy of 8.306(20) eV. This somewhat speculative assignment is nevertheless supported by the excellent agreement with the G4 and CBS-APNO calculated ionization energies of 8.25 and 8.30 eV, respectively. The ionization energy of the minor conformer II is calculated to lie ~0.05 eV below that of I, but its effect on the photoelectron spectrum is small, and the simulation also predicts a larger geometry change and, thus, a less pronounced origin transition for its spectrum.

3.2. Threshold Ionization Mass Spectra. Threshold photoionization mass spectra (see Figure 2a for representative TOF distributions) are used to plot the fractional ion abundances of parent and daughter ions in the breakdown diagram (Figure 2b).

The vanillin ion (*m/z* 152) was observed at photon energies below 12.30 eV. The first fragment ion appeared at *m/z* 151 above 11.0 eV, indicative of H loss being the lowest energy fragmentation pathway. As mentioned before, the reason for the difference between this and the much higher appearance energy observed by Betancourt et al.³³ at higher extraction field of 710 V·cm⁻¹ and a shorter acceleration region, 23 mm (vs 90 mm in the CRF-PEPICO experiment), is indicative of a kinetic shift; i.e., different residence times make the fragment observable at different effective dissociation rates and, thus,

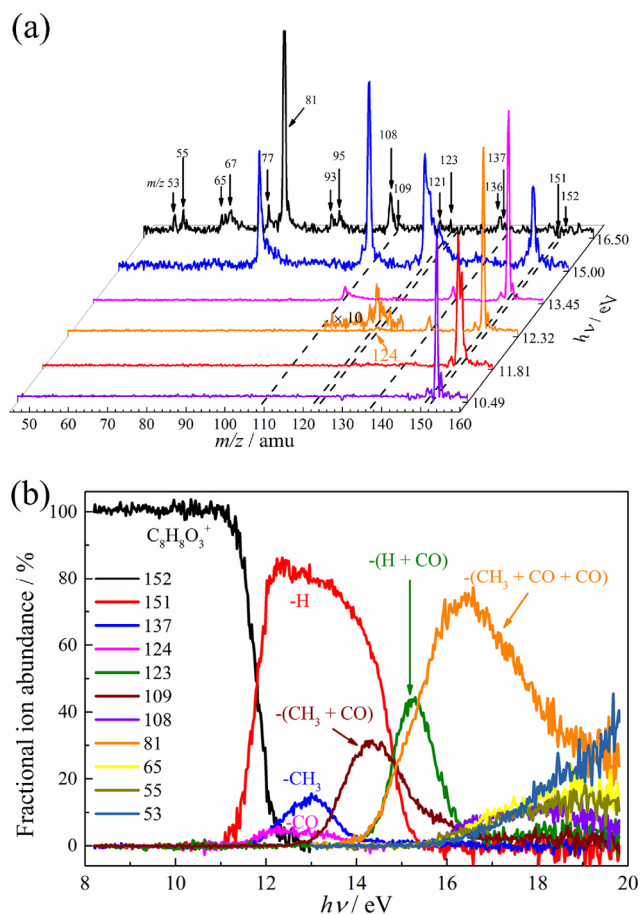


Figure 2. (a) Threshold photoionization mass spectra of vanillin at six representative photon energies. (b) Breakdown diagram of dissociative photoionization of vanillin in the 8.20–19.80 eV photon energy range.

photon energies. Considering the rate eq 3, slow dissociation rates may be the result of a large precursor density of states, i.e., a deep potential energy well in a large and/or flexible molecule, or a tight transition state. Indeed, the barrier to H loss is predicted to be 1.88 eV at the G4 level (Figure 3), and the vanillin cation is quite stable.

Slow processes taking place in the long ion acceleration region of the mass spectrometer present an asymmetric daughter ion profile tailing toward the parent ion. The dissociation rate, measurable between approximately $10^3 \text{ s}^{-1} < k < 10^7 \text{ s}^{-1}$ in our experiment, can then be determined by fitting the peak shape.⁴² This method is difficult to apply for H loss, when the asymmetry is condensed into an m/z range of 1. The center-of-gravity analysis of a baseline-separated H-loss peak or peak fitting of nearly baseline-separated parent and fragment peaks can still give insights into the rate constant.^{67,68} However, in the 151–152 m/z range, the two peaks are not baseline separated in our spectrum, and the band center analysis only yields the breakdown diagram, practically unaffected by the dissociation rate constant.⁵³ Hence, we recorded the H-loss breakdown diagram at a reduced extraction electric field of $108 \text{ V}\cdot\text{cm}^{-1}$, as well, which leads to an increased ion residence time in the acceleration region and provides a delayed snapshot of the dissociation. Thus, the red shift in the breakdown diagram upon lowering the extraction field is used to establish the fragmentation rate curve.

The second and third fragment ions are the 28 amu loss product (m/z 124, corresponding to CO loss, i.e., $\text{C}_7\text{H}_8\text{O}_2^+$, see later) and the CH_3 -loss product (m/z 137, $\text{C}_7\text{H}_5\text{O}_3^+$), both of which were observed starting at 11.6 eV. With increasing photon energy, other fragment ions also appeared, such as m/z 109 ($\text{C}_6\text{H}_5\text{O}_2^+$, $\text{CH}_3 + \text{CO}$ loss), m/z 123 ($\text{C}_7\text{H}_7\text{O}_2^+$, H + CO loss), and m/z 81 ($\text{C}_5\text{H}_5\text{O}^+$, $\text{CH}_3 + \text{CO} + \text{CO}$ loss). As shown in Figure 2a, these three ions (m/z 109, 123, and 81) exhibit variously asymmetric TOF profiles at 13.45 and 15.00 eV, indicating a tight transition state or a stable precursor ion along the corresponding decomposition pathway. This also confirms these dissociation processes to be sequential ones, as their precursor has to be metastable and the vanillin cation dissociates promptly at these energies. Yet more fragment ions appeared at m/z 136, 121, 108, 95, 93, 77, 67, 65, 55, and 53 above 16 eV. These new fragments appeared at almost the same photon energy, indicating a single or few rate-determining transition states close in energy. However, the experimental data were insufficient to propose a dissociation mechanism, and only fragments with >5% fractional abundance are plotted in the breakdown diagram.

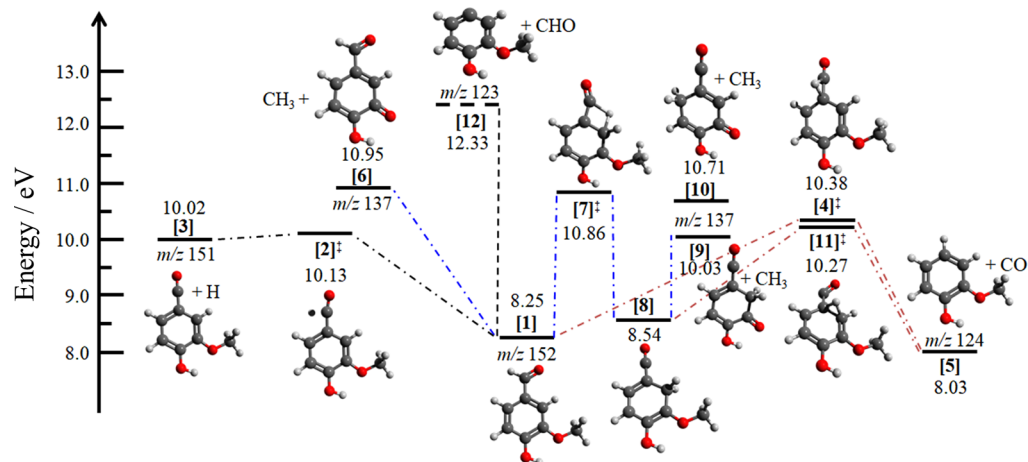


Figure 3. Primary fragmentation pathways of vanillin cation to produce the fragment ions m/z 151, 137 and 124, as well as CHO loss by direct C–C bond fission. Energies are relative to neutral vanillin and calculated with the G4 composite method.

Slightly above 12.30 eV, the parent vanillin ions disappear, and the three primary fragment ion peaks dominate the spectrum. The m/z 151, 137, and 124 signals rise in the same energy range as parallel processes. With increasing photon energy, they gradually diminish in intensity as sequential pathways open up. The m/z 137 and 124 ions decrease simultaneously and in concert with the formation of the m/z 109 fragment ion, indicating that m/z 137 and 124 ions can both fragment to the same product, $C_6H_5O_2^+$ (m/z 109), by $CH_3 + CO$ loss and $CO + CH_3$ loss from vanillin, respectively. At ~ 14.0 eV, the m/z 109 ion abundance reaches its maximum, after which the m/z 109 signal is depleted by a second CO loss yielding $C_5H_5O^+$ at m/z 81. Meanwhile, in the same energy range, a consecutive CO loss from the primary H-loss product at m/z 151 results in the rising abundance of the $C_7H_7O_2^+$ fragment ion at m/z 123. As indicated by the correlation of the breakdown curves, the high-energy fragments seen above 16.0 eV are formed in the decomposition of the $C_5H_5O^+$ (m/z 81) and $C_7H_7O_2^+$ (m/z 123) ions. The breakdown diagram shows clearly that vanillin has three primary fragment ions and they disappear from the threshold ionization spectrum in sequential fragmentation processes above 16 eV. This is at odds with the DPI free energy calculations of Betancourt et al.,³³ who proposed six primary fragment ions by considering H, CH_3 , and CHO as leaving groups with the charge on the ring or on the leaving group. Furthermore, the breakdown diagram suggests that 29 amu loss in fact corresponds to sequential H + CO loss. In order to verify these assumptions, we explored the dissociative photoionization processes using quantum chemical calculations.

3.3. Primary Decomposition Pathways of the Vanillin Cation. The complementary approach of experimental data analysis, statistical modeling, and potential energy surface calculations can provide most insights into the fragmentation mechanism.^{28,69,70} Potential energy surface exploration is guided by the experimental data to reveal reaction coordinates consistent with the observed fragmentation channels as a function of parent ion internal energy. We have explored multiple bond breaking and isomerization pathways and only report those that appear likely or possible in comparison with the experimental observations. The phase space volume is dominated by that of the ground electronic state. Therefore and because of fast and efficient internal conversion to the ground electronic state, the decomposition of valence-ionized medium-sized cations normally takes place statistically unless repulsive reaction coordinates or isolated states are involved.⁴⁰ The isomerization barrier between the two cationic conformers I and II is on the order of 60 meV, and although the two are practically isoenergetic, vertical transitions are likely to yield the conformer I, which is plotted as [1] in the following potential energy diagrams.

Figure 3 displays the primary fragmentation pathways of the vanillin cation to produce the m/z 151, 137, 124, and 123 fragment ions. The lowest-energy decomposition channel to $C_8H_7O_3^+$ (m/z 151) + H has an 0.11 eV reverse barrier with a loose transition state [2][‡] at a barrier of 1.88 eV. Along this pathway, the hydrogen atom of the aldehyde group rotates out of the benzene ring plane and the C–H bond ruptures as the C–C=O moiety becomes linear. Hydrogen atom loss from the methyl group (not shown in Figure 3) has a much higher barrier of 3.31 eV, relative to the cation, and is not expected to compete effectively. The phenolic OH hydrogen, the one proposed by Betancourt et al. to be lost,³³ can be cleaved off at

an even higher barrier at 3.56 eV, and the hydrogens on benzene are bound by close to 5.0 eV. The removal of the phenyl hydrogens yields a triplet fragment ion; all the other H-loss products are calculated to be more stable in the singlet spin state.

CO and CH_3 loss fragment ions appear in the same energy range, i.e., in parallel with hydrogen atom loss. As shown in Figure 3, CO-loss from the aldehyde group can form the m/z 124 ion [5], i.e., the guaiacol cation, via a H-migration transition state [4][‡] over a 2.13 eV barrier. The whole pathway is exothermic by 0.22 eV from the parent [1] and may involve large kinetic energy release because of the 2.3 eV reverse barrier. CO loss may also take place by a two-step hydrogen migration by [1] \rightarrow [7][‡] \rightarrow [8] \rightarrow [11][‡] \rightarrow [5] + CO. The intermediate ion [8] can be produced by a H-migration of aldehyde group to the vicinal carbon atom via transition state [7][‡] with a barrier of 2.61 eV, i.e., 0.48 eV higher than the direct H-migration path. The second H migration step takes place simultaneously with CO loss over transition state [11][‡] at 10.27 eV. Feasible rate-determining barriers for the CO-loss pathways are, thus, at 10.38 eV, [4][‡], and 10.86 eV, [7][‡]. As will be shown later, the former agrees with the experimentally determined appearance energy, E_0 .

We have found three CH_3 -loss pathways to yield the m/z 137 fragment ion. (i) Simple C–C bond fission can directly produce the m/z 137 ion [6] without a reverse barrier at 10.95 eV (2.70 eV from the parent ion). This mechanism is discussed by Betancourt et al.,³³ who report a calculated DPI free energy of 10.97 eV. (ii) Alternatively, H migration from the aldehyde group to the β -carbon of benzene ring can precede CH_3 loss from the methoxy group by [1] \rightarrow [7][‡] \rightarrow [8] \rightarrow [9] (m/z 137) + CH_3 . This path is only endothermic by 1.78 eV with a barrier [7][‡] at 10.86 eV (2.61 eV from [1]). (iii) A path at a comparable barrier starts with H migration to the other carbon with a barrier at 10.80 eV and yields [1] \rightarrow [10] (m/z 137) + CH_3 (path not shown in Figure 3). It is worth noting that the critical frequencies of these H-migration transition states are on the order of 1400 cm^{-1} (B3LYP value from G4 calculation), indicating that quantum tunneling may play a considerable role in the dynamics at low energies and may reduce the apparent E_0 for the fragment ions to below the transition state energy.

Remarkably, Figure 3 shows that H loss requires less energy than H transfer in the parent cation. A counterintuitively high H transfer activation energy has previously been reported in amines and in nitril hydride^{71,72} and raises the possibility of a roaming transition state,⁷³ in which the hydrogen almost leaves the ionic core before returning over a lower transition state, thus enabling methyl loss at a lower energy than the close-by H-transfer TS. Figure 4 shows the calculated potential energy curves along the C–H bond breaking coordinates when the aldehyde hydrogen bound to C1 (vanillin cation) is removed and approaches C3, C6, and C7 thereafter (see Figure 1) at the B3LYP/6-311G++(d,p) level. The potential energy surface becomes very flat above a C–H bond length of 2.5 Å, which could indeed provide an opportunity to the hydrogen atom to leave the aldehyde group, roam around the benzene ring, and bind to any of these carbons. It could then yield various methyl-loss fragment ions at m/z 137. The G4-calculated transition state for H migration back to C3 and C7 is 10.07 and 10.08 eV, and the corresponding CH_3 -loss products are [9] and [10], respectively. Thus, the roaming methyl-loss pathways have a lower activation energy than the H-transfer processes shown in Figure 3. However, when the leaving H

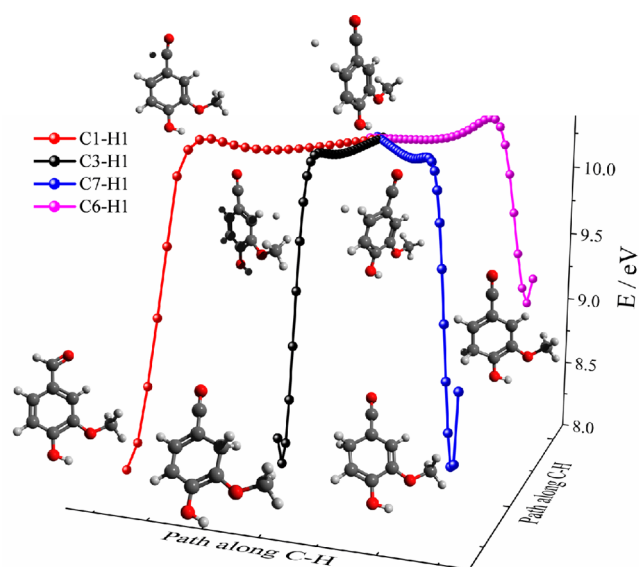


Figure 4. Calculated potential energy curves of the hydrogen atom dissociated from the C1 and associated with the C3, C7, and C6 positions of vanillin cation at the B3LYP/6-311++G(d,p) level of theory.

passes $[2]^{\ddagger}$, it finds itself on a repulsive part of the potential energy surface and the kinetic energy in the reaction coordinate will increase accordingly. In the absence of a bound minimum or a stabilizing matrix, in which vibrational energy redistribution could take place, it is unlikely that the H turns back and attacks a carbon in the benzene ring. Thus, despite the existence of a low-lying methyl-loss path, $[2]^{\ddagger}$ will predominantly yield the H-loss product. Especially at high energies, direct C–O bond cleavage is expected to form the dominant methyl-loss product, $[6]$, at m/z 137.

Finally, direct C–C bond cleavage to produce $C_7H_7O_2^+$ $[12]$ + CHO is the lowest-energy pathway we found to yield the m/z 123 fragment ion, which is computed to be a triplet in the ground state. The computed E_0 , 12.33 eV, is 2.21 eV higher than that of the H-loss pathway ($[1] \rightarrow [2]^{\ddagger} \rightarrow [3] + H$). The TOF profile of m/z 123 is clearly asymmetric at its appearance (Figure 2a), indicating that its precursor is metastable. At 14 eV, the parent ion already dissociates quickly, and based on the

abundance of the H-loss fragment at m/z 151 in this energy range, the m/z 123 ion must be a sequential dissociation product of the primary H-loss fragment ion $[3]$. Note that if multiple channels contributed to m/z 123 formation, it would likely be seen in the breakdown diagram, as well.⁵⁴

3.4. Sequential Dissociation Pathways. As indicated by the breakdown diagram in Figure 2b, the primary fragment ions at m/z 151, 137, and 124 decompose in sequential dissociation processes at higher photon energies. According to threshold energies and dynamics considerations, $[3]$, $[6]$, and $[5]$ are expected to be the predominant fragment ion isomers for m/z 151, 137, and 124, respectively. Figure 5 gives an overview of the lowest-energy sequential decomposition pathways. Direct C–C bond breaking in $[3]$ leads to the CO-loss product $[12]$ at m/z 123. Because of the strong bond, the potential energy well of the H-loss intermediate $[3]$ is deep, resulting in a high density of states and, consequently, low dissociation rate constant at threshold. This agrees with the experimental observation of metastable $[3]$ and asymmetric TOF distributions for $[12]$ close to its appearance in the breakdown diagram, indicative of a large kinetic shift. At even higher energies, the secondary fragment ion $[12]$ can further lose a methyl group and yield $[13]$ at m/z 108. No significant reverse barriers were found along these simple bond breaking processes, as opposed to the alternative and unlikely reaction pathway to yield another m/z 108 fragment isomer, $[25]$ (see below).

The m/z 109 ion $[18]$ is produced from both primary fragments m/z 124 $[5]$ and 137 $[6]$. As shown in Figure 5, O–CH₃ bond breaking in the guaiacol cation $[5]$ leads to $[18]$ directly over a barrier of 2.59 eV relative to $[5]$. Alternatively, isomerization and decomposition reactions from the methyl-loss primary product also yield $[18]$. The lowest energy channel from $[6]$ to $[18]$ + CO is $[6] \rightarrow [14]^{\ddagger} \rightarrow [10] \rightarrow [15]^{\ddagger} \rightarrow [16] \rightarrow [17]^{\ddagger} \rightarrow [18]$, as shown in Figure 5. The m/z 109 ions appear at ~ 13 eV experimentally, which is much higher than the theoretically predicted CO-loss threshold from $[5]$ but is quite close to the 12.82 eV thermochemical threshold for $[1] \rightarrow [6] + CH_3 \rightarrow [18] + CH_3 + CO$. Also, the abundance of m/z 137 exceeds that of m/z 124 above 12.2 eV (Figure 2b), which clearly indicates that the CH₃-loss fragment ion, $[6]$, is dominant at higher photon energies in comparison

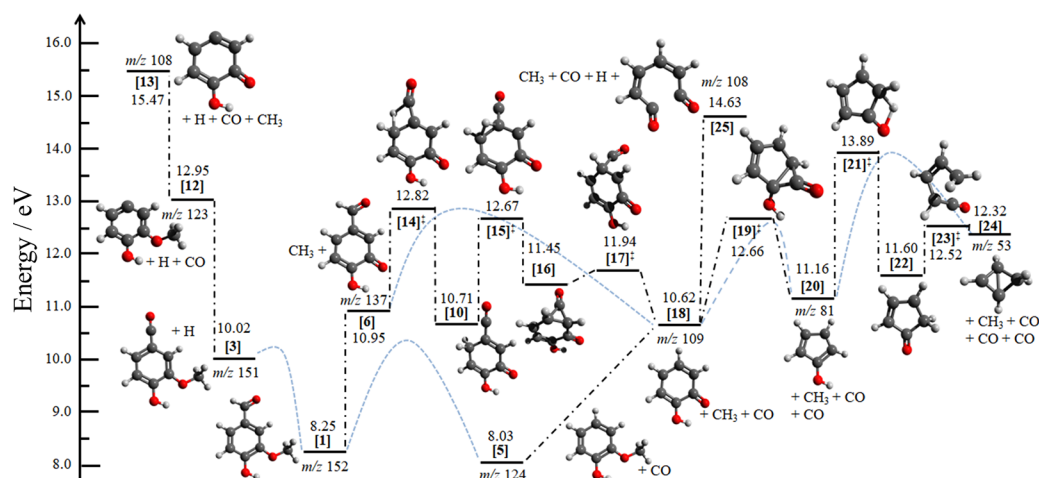


Figure 5. Sequential decomposition pathways of the primary fragment ions of vanillin: $[3]$, $[6]$, and $[5]$. The G4 energies are given relative to the conformer I $[1]$ of neutral vanillin.

to the CO-loss product, [5], although the barrier to CO loss is in fact lower. Furthermore, there is a large reverse barrier along the primary CO-loss pathway of [1] \rightarrow [5] + CO, meaning that large kinetic energy release can stabilize the resulting guaiacol cation.

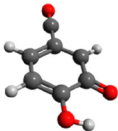
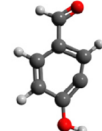
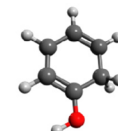
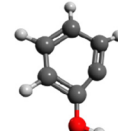
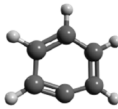
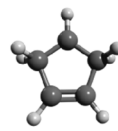
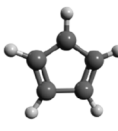
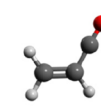
Once high internal energy [18] is formed, decarbonylation produces the hydroxycyclopentadienyl cation [20] (m/z 81) via transition state [19][‡] at a barrier of 2.04 eV, similar to the thermal decomposition of neutral radicals of [18].^{20,74} Subsequently, a ring-opening of [20] leads to the formation of the C₄H₅⁺ ion [24] at m/z 53 by a further CO loss over the rate-determining transition state [21][‡] at a barrier of 2.73 eV. While [18] may lose a hydrogen atom to form the m/z 108 fragment [25] at 3.99 eV barrier by direct O–H bond breaking, this process is unlikely as the m/z 108 peak is absent in the electron ionization mass spectrum of guaiacol.⁷⁵

The fragmentation mechanism cannot be unambiguously determined for the remaining daughter ions appearing at low abundance above 16 eV photon energy. We list calculated thermochemical thresholds to some of them in Table 1. As can be seen, the formation of these fragments is probably accompanied by further sizable reverse barriers, which make it difficult to argue for a definitive formation mechanism.

3.5. Dissociative Photoionization Model. On the basis of the insights gained by the analysis of the TOF distributions, the breakdown diagram, and the potential energy surface, a statistical decomposition model was built for the major fragmentation pathways. As shown in Figure 5, CO + CH₃-loss products can be formed via various pathways involving different primary and sequential decompositions. At photon energies above 16 eV, the numerous but weak fragment ion signals preclude a detailed analysis. Fragmentation processes involving a sizable reverse barrier involve suprathermal kinetic energy release. While there are experimental^{76–78} and theoretical²⁸ approaches to address this quantitatively, we do not expect them to reveal substantially more accurate energetics than offered by quantum chemical calculations for vanillin. Consequently, we only included the three primary fragmentation pathways as well as the sequential dissociations from the H-loss fragment, i.e., H, CO, CH₃, H + CO, and H + CO + CH₃ loss, in the statistical model to derive experimental 0 K appearance energies, E_0 , for the four decomposition channels.

As shown in Figure 6, the breakdown curves were reproduced faithfully by the model, which supports the argument that these processes take place statistically. While the parallel CH₃- and CO-loss channels deliver some rate information, the bulk of it is hidden in the unresolved H-loss peak. As discussed previously, we can verify and establish the kinetic shift by recording the breakdown diagram at a lower extraction field, 108 V·cm⁻¹, thereby lengthening the time the parent ions spend in the acceleration region. The breakdown curves shift to a lower energy and are reproduced by the same statistical model with the revised ion optics parameters as well (dashed lines in Figure 6). This confirms H loss from the vanillin cation to be a slow process at threshold and the resulting, large kinetic shift for this pathway. For hydrogen atom loss, the lowest-energy decomposition channel, the $E_0(\text{C}_8\text{H}_7\text{O}_3^+/\text{C}_8\text{H}_8\text{O}_3, m/z$ 151), was determined to be 10.13 \pm 0.01 eV. This value agrees perfectly with the theoretically predicted activation energy of [2][‡] of 10.13 eV. This serendipitous agreement may be due to error cancellation, as quantum tunneling probably contributes to the fragmentation

Table 1. Tentative Structures and Thermochemical Limits of the Minor m/z 136, 121, 95, 93, 67, 65, and 55 Fragment Ions Involved in High-Energy Dissociative Photoionization of Vanillin at the G4 Level^a

m/z	Tentative fragment ion	Neutral fragments	Energy / eV
136		H + CH ₃	13.19
121		OCH ₃	13.24
95		CO + CHO	9.77
93		CO + OCH ₃	13.15
77		CO + CH ₂ O + OH	13.62
67		CO + CHO + CO	11.59
65		CO + OCH ₃ + CO	12.80
55		CH ₃ + CO + CO + C ₂ H ₂	13.13

^aThe m/z 65 fragment ion is a triplet, and the remaining odd-mass fragment ions are singlets in the ground state.

and has not been considered. This also confirms the large kinetic shift, i.e., the excess energy needed for even zero internal energy neutrals to dissociate on the experimental time scale, at 2.1 eV.

Parallel to H loss, CO and CH₃ loss leads to the minor m/z 124 and 137 fragment ion peaks seen only below 14 eV (Table 2). Their slowly rising intensities are indicative of a competitive shift; i.e., their rate constants rise more quickly than that of H loss with energy but not much more so. On the basis of the statistical model, the dissociation thresholds of

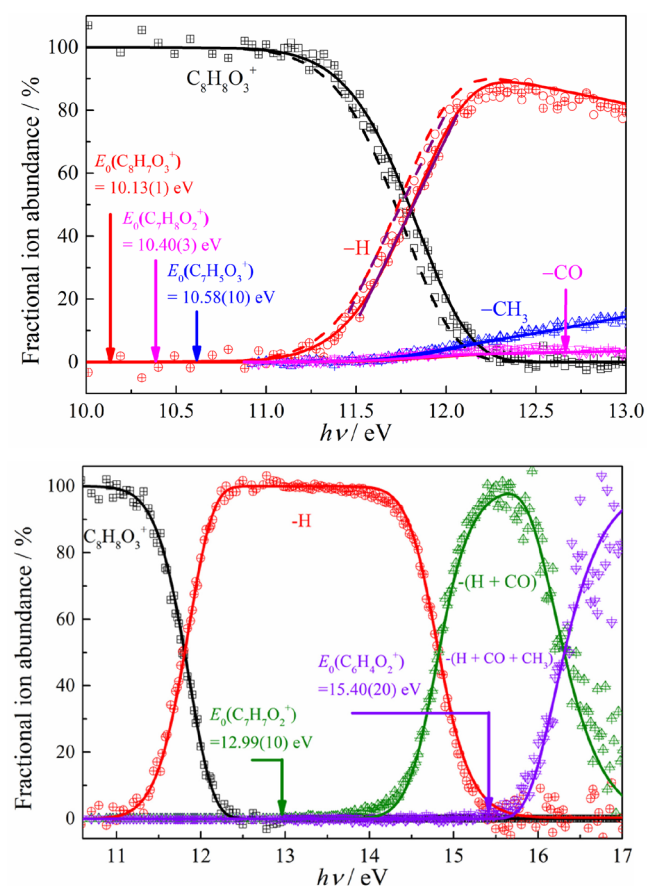


Figure 6. Statistical modeling of the lowest three decomposition pathways of vanillin cation (top) and the model including sequential CO loss from m/z 151 leading to m/z 123 and CH_3 loss from m/z 123 leading to m/z 108 (bottom). Open symbols represent the experimental fractional abundances, and the solid lines show the simulated results with the statistical model. The 0 K appearance energies of the three primary fragment ions were derived and noted with the arrows.

Table 2. Experimental and G4-Computed 0 K Ionization and Appearance Energies for the Modeled Dissociative Photoionization Processes of Vanillin

m/z	neutral fragment(s)	exptl, eV	calcd, eV
152		8.306(20)	8.25
151	H	10.13(1)	10.13
124	CO	10.40(3)	10.38
137	CH_3	10.58(10)	10.86
123	H + CO	12.99(10)	12.95
108	H + CO + CH_3	15.40(20)	15.47

these two channels are $E_0(\text{C}_7\text{H}_8\text{O}_2^+/\text{C}_8\text{H}_8\text{O}_3, m/z 124) = 10.40(3)$ eV and $E_0(\text{C}_7\text{H}_5\text{O}_3^+/\text{C}_8\text{H}_8\text{O}_3, m/z 137) = 10.58(10)$ eV.

The former agrees very well with the G4-calculated threshold to guaiacol cation formation at 10.38 eV and provides strong evidence for the $[1] \rightarrow [4]^\ddagger \rightarrow [6] + \text{CO}$ mechanism. The latter is below the computed thresholds of 10.95 eV for direct bond breaking to $[6] + \text{CH}_3$ and 10.80 or 10.86 eV for the isomerization-mediated pathway to $[10] + \text{CH}_3$ or $[9] + \text{CH}_3$. However, when considering that tunneling may easily suppress the apparent barrier by 100 meV⁶⁷ and the potential, minor contribution of the roaming methyl loss close

to threshold, the experimental and computational results are in fact in good agreement. Sequential CO loss from m/z 151 to produce the m/z 123 fragment ion and sequential CH_3 loss from m/z 123 to produce m/z 108 were also modeled. These are plotted in Figure 6 in a separate breakdown diagram, renormalized to include only the parent and the three sequential fragment ions, i.e., the H-loss, (H + CO)-loss, and the (H + CO + CH_3)-loss fragment ions. The modeling yielded $E_0(\text{C}_7\text{H}_7\text{O}_2^+/\text{C}_8\text{H}_8\text{O}_3, m/z 123) = 12.99(10)$ eV and $E_0(\text{C}_6\text{H}_4\text{O}_2^+/\text{C}_8\text{H}_8\text{O}_3, m/z 108) = 15.40(20)$ eV, respectively, which agree well with the G4-calculated threshold to $[12]$ at 12.95 eV and $[13]$ at 15.47 eV, respectively, confirming the proposed mechanism.

3.6. Computational Thermochemistry. The uncertainty of the fitted appearance energies is affected by the large kinetic and competitive shifts. Furthermore, thresholds to kinetically controlled DPI processes cannot be used in ion cycles either.⁴⁰ However, reaction energetics may determine branching ratios and drive selectivity both in noncatalytic and in catalytic processes. Indeed, as reviewed below, experimental research on the benzene derivatives' thermochemistry has been flourishing recently. Yet, we were surprised by the relative lack of computed energetics, particularly that subchemical accuracy (≤ 1 kJ mol⁻¹) is getting within reach with the help of isodesmic reaction energy calculations.^{79,80}

The enthalpy of formation of crystalline vanillin was reported as $\Delta_f H^\circ_{298\text{K}}(\text{vanillin, cr}) = -477.0 \pm 0.8$, -475.5 ± 1.5 , and -478.3 ± 2.0 kJ mol⁻¹ by Lebedeva et al.,⁸¹ Maksimuk et al.,⁸² and Almeida et al.,⁸³ respectively. Almeida et al. also report standard sublimation enthalpies 99.6 ± 0.2 and, on average, 88.4 kJ mol⁻¹ based on their differential heat capacity measurements and literature vapor pressures, respectively. The reason for this discrepancy being unknown, we can combine both sublimation enthalpies with the solid-phase vanillin enthalpy of formation of Lebedeva et al. to obtain $\Delta_f H^\circ_{298\text{K}}(\text{vanillin, g}) = -377.4$ or -388.6 kJ mol⁻¹. Maksimuk et al. also used density functional and G3 theory in empirically corrected atomization energy calculations and reported a computed $\Delta_f H^\circ_{298\text{K}}(\text{vanillin, g}) = -375.8 \pm 2.1$ kJ mol⁻¹. Almeida et al. carried out reaction energy calculations for unspecified reactions at the G3(MP2)//B3LYP level of theory and arrived at $\Delta_f H^\circ_{298\text{K}}(\text{vanillin, g}) = -375.1 \pm 9.4$ kJ mol⁻¹, taking the 0.6 kJ mol⁻¹ increase in the thermal enthalpy due to conformer II explicitly into account.

The Active Thermochemical Tables (ATcT) list enthalpies of formation for benzene and the monofunctionalized benzene derivatives phenol, benzaldehyde, and anisole (Figure 7).⁸⁴ We point out that the phenol enthalpy of formation is listed as -96.4 ± 0.9 kJ mol⁻¹ in the Pedley compendium.⁸⁵ Anisole is a subject of a more recent work by Simoes et al.,⁸⁶ in which a remeasured anisole combustion and vaporization enthalpy yielded -70.7 ± 1.4 kJ mol⁻¹, which is higher than the ATcT value, but their error bars overlap. However, past measurements with smaller error bars appear to confirm the ATcT value, and the main goal of Simoes et al. may have been not to supersede these but to establish beyond doubt that the Mulder et al. value⁸⁷ of -76.7 kJ mol⁻¹ was too low, whereas that of Pedley was too high at -67.9 kJ mol⁻¹.⁸⁵

Therefore, we rely on version 1.122p of ATcT for ancillary gas-phase heats of formation of four compounds (Figure 7) to set up isodesmic functional group transfer reactions to connect the monofunctionalized and the bi-/trifunctionalized derivatives:

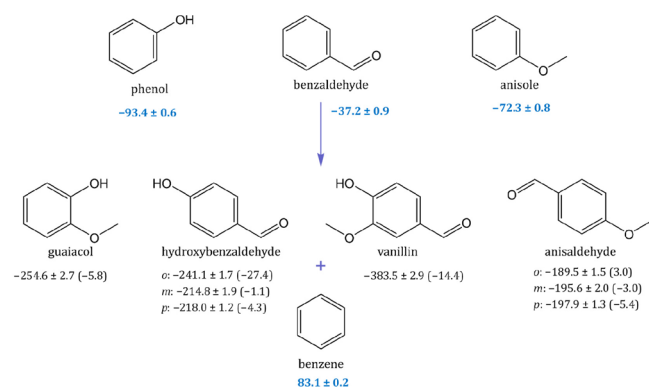
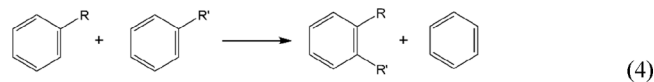


Figure 7. Standard room temperature enthalpies of formation of bi- and trifunctionalized benzene derivatives based on reference data from the Active Thermochemical Tables (in blue) and isodesmic reaction energy calculations. The enthalpies of formation can be approximated by simple group additivity with -176.5 , -120.3 , and $-155.4 \text{ kJ mol}^{-1}$ added for each $\text{R} = \text{OH}$, CHO , and OCH_3 group, respectively, to the benzene heat of formation. The differences of the calculated heat of formation and the group additivity value are given in parentheses.



We used G4 and CBS-QB3 theories to calculate the 0 K energy and the thermal enthalpy of four low-energy conformers of *m*-hydroxybenzaldehyde (1.4) and *m*-anisaldehyde (1.5) as well as two conformers of *p*-hydroxybenzaldehyde (0.2), *p*-anisaldehyde (0.1), and vanillin (0.6), within 5 kJ mol^{-1} of the global minimum. The conformational zero-point and thermal enthalpies were used to estimate the effect of the room temperature conformational equilibrium on the thermal enthalpy of each species, similar to the approach of Almeida et al.⁸³ and our work on halocyclohexanes.⁸⁸ These corrections are given here in kJ mol^{-1} in parentheses for each of these samples. The effect of large-amplitude motions, such as internal hindered rotation, on the thermal enthalpy is also a legitimate concern.⁸⁹ In order to ensure a consistent approach, we calculated the average contribution of internal rotation to the thermal enthalpy using Pitzer rotors and McClurg's density of states interpolation function.^{90–92} The corrected thermal enthalpies were 0.4 kJ mol^{-1} higher and 0.2 kJ mol^{-1} lower than the ATcT ones for anisole and phenol, respectively, and were used to convert the ATcT 0 K values to 298 K in Figure 7. The hindered rotor correction to the isodesmic reaction energies was no more than 0.1 kJ mol^{-1} except for *o*-hydroxybenzaldehyde, for which it was 0.2 kJ mol^{-1} because of a loss of a hindered rotor because of the strong intramolecular hydrogen bond. Thus, thermal errors are expected to be minor and dominated by error propagation from the thermochemical anchors. CBS-APNO and W1 calculations were applied to the most stable conformer only, and the average G4, CBS-QB3, CBS-APNO, and W1 isodesmic reaction energy was used to calculate the enthalpy of formation of the bi- and trifunctionalized benzene species in Figure 7. The reported uncertainties assume error propagation of the ATcT heats of formation as well as twice the standard deviation of the reaction energy calculated at the four levels of theory, with the difference between the average and the W1-based heat of formation and the uncertainty in the hindered rotor calculations as added uncertainty.

Varfolomeev et al. reported the standard heat of formation of gaseous guaiacol as $-247.3 \pm 1.8 \text{ kJ mol}^{-1}$,⁹³ based on their heat of vaporization and the heat of combustion reported by Matos et al.⁹⁴ This is significantly higher than our computed value of $-254.6 \pm 2.7 \text{ kJ mol}^{-1}$. However, they also reported a $-255.0 \text{ kJ mol}^{-1}$ value, based on the G3MP2 atomization energy, as well as $-251.0 \text{ kJ mol}^{-1}$ based on a functional group transfer reaction energy, similar to eq 4, relying on the Pedley compendium⁸⁵ for ancillary values. On the basis of the most reliable ATcT ancillary values, this corresponds to $-253.2 \text{ kJ mol}^{-1}$. In short, the computational values are consistent but differ markedly from the experimental one. It is unclear whether this can be explained by an error in the vaporization enthalpy, which, as reviewed by Varfolomeev et al.,⁹³ spans the $58.9\text{--}61.4 \text{ kJ mol}^{-1}$ range, inconsistent with their average 0.4 kJ mol^{-1} error bar, by an error in the combustion enthalpy measurement or, unlikely, by a hitherto neglected quantum chemical effect in the calculations.

The enthalpy of formation *ortho*-hydroxybenzaldehyde has been reported as $-238.3 \pm 2.5 \text{ kJ mol}^{-1}$ and $-245.6 \pm 2.2 \text{ kJ mol}^{-1}$ by Bernardes and Minas da Piedade⁹⁵ and by Ribeiro da Silva and Araújo,⁹⁶ respectively. Our value, $-241.1 \pm 1.7 \text{ kJ mol}^{-1}$, appears to suggest that the truth lies in the middle. Ribeiro da Silva et al. measured the gas-phase enthalpy of formation for the *meta*-hydroxybenzaldehyde isomer as $-217.8 \pm 1.4 \text{ kJ mol}^{-1}$,⁹⁷ in moderate agreement with our calculated value of $-214.8 \pm 1.9 \text{ kJ mol}^{-1}$. For the *para* isomer, Bernardes and Minas da Piedade⁹⁵ reported $-220.3 \pm 2.0 \text{ kJ mol}^{-1}$, while Ribeiro da Silva et al. measured the heat of formation in the gas phase as $-217.8 \pm 1.4 \text{ kJ mol}^{-1}$.⁹⁷ Our computed result of $-218.0 \pm 1.2 \text{ kJ mol}^{-1}$ agrees perfectly with the latter value.

We are not aware of previously reported enthalpies of formation for gaseous anisaldehyde (methoxybenzaldehyde) isomers apart from the *para* isomer, for which Pedley lists a value of $-202.7 \pm 5.4 \text{ kJ mol}^{-1}$, which is, because of its large uncertainty, in agreement with our computed $-197.9 \pm 1.3 \text{ kJ mol}^{-1}$.

As mentioned previously, the vaporization enthalpy of vanillin is not reassuringly known, and both $\Delta_{\text{v}}H_{298\text{K}}^{\circ}(\text{vanillin}, \text{g}) = -377.4$ or $-388.6 \text{ kJ mol}^{-1}$ may realistically be possible. Previously computed values cluster around -375 kJ mol^{-1} , favoring the more recent vaporization enthalpy measurement. However, our isodesmic reaction energies yield $-383.5 \pm 2.9 \text{ kJ mol}^{-1}$, which lies squarely in the middle, and in a sense lends some weight to the historic vapor pressure determination by Serpinski et al.⁹⁸

As far as we are aware, this is the first time a quantum chemical method comparable to the W1 approach has been applied to vanillin. Yet, weeks of CPU time notwithstanding, it is intriguing to see that a basic group additivity approach gets us to within 6 kJ mol^{-1} of the isodesmic reaction energy based enthalpies of formation with the notable exception of *o*-hydroxybenzaldehyde (with a strong intramolecular H-bond) and vanillin (with three functional groups apparently leading to a larger stabilization). The modest intergroup coupling also implies that the computational approaches should reproduce the small relative energy differences quite well. Indeed, the absolute difference between an isodesmic reaction energy computed using a single composite method and the average value was only 0.6 kJ mol^{-1} on average. It was largest for guaiacol at the CBS-QB3 level (1.6 kJ mol^{-1}) and vanillin at the G4 level (1.5 kJ mol^{-1}). Thus, composite methods provide a reassuringly consistent picture of the energetics of these

species. While the accuracy of our derived enthalpies of formation does not follow from this, we believe it only hinges on the accuracy of the ancillary thermochemical data and whether an important quantum chemical effect was neglected in *all* calculations.

4. CONCLUSIONS

We studied the valence photoionization of vanillin by photoelectron photoion coincidence from its ionization onset to 20 eV photon energy. The energies of the vertical ionizing transitions to the electronic ground and excited states of the dominant and the minor vanillin conformer were calculated using EOM-IP-CCSD, which reproduced the overall structure of the photoelectron spectrum well. Tentative vibrational structure of the weak, ground state band could be simulated by Franck–Condon factor calculations to determine the adiabatic ionization energy of vanillin as 8.306(20) eV. The breakdown diagram was plotted and analyzed to unveil parallel and sequential steps in the dissociative photoionization mechanism. These insights guided *ab initio* calculations to explore the reaction pathways, the results of which were used to set up a statistical model for the primary and selected sequential dissociation processes. The $C_8H_8O_3^+$ vanillin parent ion dissociates by three parallel channels to produce m/z 151 (H loss, $E_0 = 10.13$ eV vs G4 value of 10.13 eV), m/z 124 (CO loss, $E_0 = 10.40$ eV vs G4 calculated value of 10.38 eV), and m/z 137 (CH_3 loss, $E_0 = 10.58$ eV vs G4 calculated value of 10.95 eV) fragment ions. The role of tunneling and roaming was discussed for the methyl-loss channel.

The three primary fragments undergo sequential dissociation processes at higher energies. Sequential CO loss from m/z 151 leads to m/z 123 (H + CO loss, $E_0 = 12.99$ eV vs G4 threshold of 12.95 eV). Further CH_3 loss from the m/z 123 fragment ion yields m/z 108 (H + CO + CH_3 loss, $E_0 = 15.40$ eV vs G4 threshold of 15.47 eV). Although these processes take place by simple C–C bond breaking over a loose transition state, they are still metastable because of the large stability of the intermediate ions. The primary CH_3 - and CO-loss fragments at m/z 137 and 124 lose a CO or a CH_3 neutral, respectively, to form m/z 109 at a G4-computed threshold of 12.82 and 10.62 eV, respectively. The initial CO-loss is exothermic, and the large reverse barrier and the resulting kinetic energy release stabilize the intermediate guaiacol cation and enhance its abundance in the breakdown diagram. The m/z 109 fragment may lose two more CO units to form m/z 81 and 53 via multiple isomerization steps. Carbon monoxide being a very stable leaving group, the thermochemical limits to consecutive CO losses are low. However, CO loss is generally preceded by energetic and tight isomerization transition states, which determine the fragmentation dynamics and raise the appearance energies of the fragments. These mass spectrometric insights and appearance energies will aid the spectral assignment of lignin conversion spectra via catalytic pyrolysis or oxidative biphasic depolymerization approaches, in particular of vanillin chemistry.

The measured dissociative photoionization onsets' uncertainty is affected by kinetic and competitive shifts, and they rarely correspond to thermochemical thresholds. Therefore, they could not be used in ion cycle calculations to determine, for example, enthalpies of formation. However, the experimental thermochemistry of vanillin and related species has been quite active recently, mostly by bomb calorimetry and phase change studies. We set up isodesmic reactions to revisit

the enthalpies of formation of some bi- and trifunctionalized benzene derivatives and found that subchemical accuracy is often within reach for the gaseous energetics of these compounds. This may be important when selectivity and conversion are driven by energetics effects, and it also gives us confidence in evaluating the thermochemistry of analogous compounds *in silico*.

AUTHOR INFORMATION

Corresponding Authors

Xiaoguo Zhou – Hefei National Laboratory for Physical Sciences at the Microscale, Department of Chemical Physics, University of Science and Technology of China, Hefei 230026, China; orcid.org/0000-0002-0264-0146; Email: xzhou@ustc.edu.cn

Andras Bodi – Paul Scherrer Institute, 5232 Villigen, Switzerland; orcid.org/0000-0003-2742-1051; Email: andras.boedi@psi.ch

Authors

Xiangkun Wu – Paul Scherrer Institute, 5232 Villigen, Switzerland; Hefei National Laboratory for Physical Sciences at the Microscale, Department of Chemical Physics, University of Science and Technology of China, Hefei 230026, China; orcid.org/0000-0001-8515-3302

Saša Bjelić – Paul Scherrer Institute, 5232 Villigen, Switzerland; orcid.org/0000-0002-9805-3201

Patrick Hemberger – Paul Scherrer Institute, 5232 Villigen, Switzerland; orcid.org/0000-0002-1251-4549

Complete contact information is available at:

<https://pubs.acs.org/10.1021/acs.jpca.1c00876>

Notes

The authors declare no competing financial interest.

ACKNOWLEDGMENTS

Experiments were carried out at the VUV beamline of the Swiss Light Source of the Paul Scherrer Institute with support from the PSI CROSS project funding initiative. The financial support from the Swiss Federal Office for Energy (BFE Contract SI/501269-01) and the National Natural Science Foundation of China (Grants 21903079 and 21873089) is gratefully acknowledged. The work was also financially supported by the National Key Research and Development Program of China (Grant 2016YFF0200502) and the USTC-NSRL. X.W. appreciates the SSSTC scholarship (Grant EGCN 01-042018) and the China Scholarship Council (Grant 201806340001) for support.

REFERENCES

- (1) Fache, M.; Boutevin, B.; Caillol, S. Vanillin production from lignin and its use as a renewable chemical. *ACS Sustainable Chem. Eng.* **2016**, *4* (1), 35–46.
- (2) Bomgardner, M. M. Following many routes to naturally derived vanillin. *Chem. Eng. News* **2014**, *92* (6), 14.
- (3) Santosh Kumar, S.; Priyadarsini, K. I.; Sainis, K. B. Free radical scavenging activity of vanillin and o-vanillin using 1,1-diphenyl-2-picrylhydrazyl (DPPH) radical. *Redox Rep.* **2002**, *7*, 35–40.
- (4) Bruijninx, P. C.; Weckhuysen, B. M. Shale gas revolution: An opportunity for the production of biobased chemicals? *Angew. Chem., Int. Ed.* **2013**, *52* (46), 11980–11987.
- (5) Cao, L.; Yu, I. K. M.; Liu, Y.; Ruan, X.; Tsang, D. C.; Hunt, A. J.; Ok, Y. S.; Song, H.; Zhang, S. Lignin valorization for the production

of renewable chemicals: State-of-the-art review and future prospects. *Bioresour. Technol.* **2018**, *269*, 465–475.

(6) Sun, Z.; Fridrich, B.; de Santi, A.; Elangovan, S.; Barta, K. Bright side of lignin depolymerization: Toward new platform chemicals. *Chem. Rev.* **2018**, *118* (2), 614–678.

(7) Fache, M.; Boutevin, B.; Caillol, S. Vanillin, a key-intermediate of biobased polymers. *Eur. Polym. J.* **2015**, *68*, 488–502.

(8) Rahimi, A.; Azarpira, A.; Kim, H.; Ralph, J.; Stahl, S. S. Chemoselective metal-free aerobic alcohol oxidation in lignin. *J. Am. Chem. Soc.* **2013**, *135* (17), 6415–6418.

(9) Shuai, L.; Amiri, M. T.; Questell-Santiago, Y. M.; Héroguel, F.; Li, Y.; Kim, H.; Meilan, R.; Chapple, C.; Ralph, J.; Luterbacher, J. S. Formaldehyde stabilization facilitates lignin monomer production during biomass depolymerization. *Science* **2016**, *354* (6310), 329–333.

(10) Lan, W.; Amiri, M. T.; Hunston, C. M.; Luterbacher, J. S. Protection group effects during α,γ -diol lignin stabilization promote high-selectivity monomer production. *Angew. Chem.* **2018**, *130* (5), 1370–1374.

(11) Hu, J.; Zhang, Q.; Lee, D.-J. Kraft lignin biorefinery: A perspective. *Bioresour. Technol.* **2018**, *247*, 1181–1183.

(12) Achyuthan, K. E.; Achyuthan, A. M.; Adams, P. D.; Dirk, S. M.; Harper, J. C.; Simmons, B. A.; Singh, A. K. Supramolecular self-assembled chaos: Polyphenolic lignin's barrier to cost-effective lignocellulosic biofuels. *Molecules* **2010**, *15* (12), 8641–8688.

(13) Custodis, V. B.; Bährle, C.; Vogel, F.; van Bokhoven, J. A. Phenols and aromatics from fast pyrolysis of variously prepared lignins from hard- and softwoods. *J. Anal. Appl. Pyrolysis* **2015**, *115*, 214–223.

(14) Ma, Z.; Custodis, V.; van Bokhoven, J. A. Selective deoxygenation of lignin during catalytic fast pyrolysis. *Catal. Sci. Technol.* **2014**, *4* (3), 766–772.

(15) Bjelić, S.; Garbuio, L.; Arturi, K. R.; van Bokhoven, J. A.; Jeschke, G.; Vogel, F. Oxidative biphasic depolymerization (bpd) of kraft lignin at low pH. *ChemistrySelect* **2018**, *3* (41), 11680–11686.

(16) Zirbes, M.; Quadri, L. L.; Breiner, M.; Stenglein, A.; Bomm, A.; Schade, W.; Waldvogel, S. R. High-temperature electrolysis of kraft lignin for selective vanillin formation. *ACS Sustainable Chem. Eng.* **2020**, *8* (19), 7300–7307.

(17) Zakzeski, J.; Buijinninx, P. C.; Jongerius, A. L.; Weckhuysen, B. M. The catalytic valorization of lignin for the production of renewable chemicals. *Chem. Rev.* **2010**, *110* (6), 3552–3599.

(18) Tomlinson, G. H., 2nd; Hibbert, H. Studies on lignin and related compounds. Xv. Mechanism of vanillin formation from spruce lignin sulfonic acids in relation to lignin structure I. *J. Am. Chem. Soc.* **1936**, *58* (2), 348–353.

(19) Wilson, K. R.; Qi, F. Probing chemistry at vacuum ultraviolet synchrotron light sources. In *Photoionization and Photo-Induced Processes in Mass Spectrometry*; Wiley-VCH Verlag GmbH & Co. KGaA: Weinheim, Germany, 2021; pp 159–213.

(20) Custodis, V. B. F.; Hemberger, P.; Ma, Z.; Van Bokhoven, J. A. Mechanism of fast pyrolysis of lignin: Studying model compounds. *J. Phys. Chem. B* **2014**, *118* (29), 8524–31.

(21) Custodis, V. B.; Hemberger, P.; van Bokhoven, J. A. How inter- and intramolecular reactions dominate the formation of products in lignin pyrolysis. *Chem. - Eur. J.* **2017**, *23* (36), 8658–8668.

(22) Hemberger, P.; Custodis, V. B.; Bodi, A.; Gerber, T.; van Bokhoven, J. A. Understanding the mechanism of catalytic fast pyrolysis by unveiling reactive intermediates in heterogeneous catalysis. *Nat. Commun.* **2017**, *8* (1), 15946.

(23) Bodi, A.; Hemberger, P.; Osborn, D. L.; Sztáray, B. I. Mass-resolved isomer-selective chemical analysis with imaging photoelectron photoion coincidence spectroscopy. *J. Phys. Chem. Lett.* **2013**, *4* (17), 2948–2952.

(24) Bouwman, J.; Bodi, A.; Hemberger, P. Nitrogen matters: The difference between panh and pah formation. *Phys. Chem. Chem. Phys.* **2018**, *20* (47), 29910–29917.

(25) Hemberger, P.; Pan, Z.; Bodi, A.; van Bokhoven, J. A.; Ormond, T. K.; Ellison, G. B.; Genossar, N.; Baraban, J. H. The threshold

photoelectron spectrum of fulvenone: A reactive ketene derivative in lignin valorization. *ChemPhysChem* **2020**, *21* (19), 2217–2222.

(26) Hemberger, P.; van Bokhoven, J. A.; Pérez-Ramírez, J.; Bodi, A. New analytical tools for advanced mechanistic studies in catalysis: Photoionization and photoelectron photoion coincidence spectroscopy. *Catal. Sci. Technol.* **2020**, *10* (7), 1975–1990.

(27) Heringa, M. F.; Slowik, J. G.; Prévôt, A. S.; Baltensperger, U.; Hemberger, P.; Bodi, A. Dissociative ionization mechanism and appearance energies in adipic acid revealed by imaging photoelectron photoion coincidence, selective deuteration, and calculations. *J. Phys. Chem. A* **2016**, *120* (20), 3397–3405.

(28) Majer, K.; Signorell, R.; Heringa, M. F.; Goldmann, M.; Hemberger, P.; Bodi, A. Valence photoionization of thymine: Ionization energies, vibrational structure, and fragmentation pathways from the slow to the ultrafast. *Chem. - Eur. J.* **2019**, *25*, 14192–14204.

(29) Rinesch, T.; Mottweiler, J.; Puche, M.; Concepción, P.; Corma, A.; Bolm, C. Mechanistic investigation of the catalyzed cleavage for the lignin β -O-4 linkage: Implications for vanillin and vanillic acid formation. *ACS Sustainable Chem. Eng.* **2017**, *5* (11), 9818–9825.

(30) Takahashi, L. K.; Zhou, J.; Kostko, O.; Golan, A.; Leone, S. R.; Ahmed, M. Vacuum-ultraviolet photoionization and mass spectrometric characterization of lignin monomers coniferyl and sinapyl alcohols. *J. Phys. Chem. A* **2011**, *115* (15), 3279–3290.

(31) Ponomarev, D.; Sergeev, Y. L. Oxidation potential of compounds modeling lignin as a measure of their oxidative capacity. *Chem. Nat. Compd.* **1982**, *18* (6), 764–765.

(32) Shu, X.; Yang, B.; Meng, J.; Wang, Y.; Shu, J. Vacuum ultraviolet photoionization mass spectra of typical organics contained in ambient aerosols. *Spectrosc. Lett.* **2013**, *46* (3), 227–234.

(33) Moreno Betancourt, A.; Coutinho, L. H.; Bernini, R. B.; de Moura, C. E. V.; Rocha, A. B.; de Souza, G. G. B. Vuv and soft x-ray ionization of a plant volatile vanillin ($C_8H_8O_3$). *J. Chem. Phys.* **2016**, *144*, 114305.

(34) Lifshitz, C. Time-resolved appearance energies, breakdown graphs, and mass spectra: The elusive “kinetic shift”. *Mass Spectrom. Rev.* **1982**, *1* (4), 309–348.

(35) Sztáray, B.; Bodi, A.; Baer, T. Modeling unimolecular reactions in photoelectron photoion coincidence experiments. *J. Mass Spectrom.* **2010**, *45* (11), 1233–1245.

(36) Wu, X.; Zhou, X.; Hemberger, P.; Bodi, A. Dissociative photoionization of dimethyl carbonate: The more it is cut, the bigger the fragment ion. *J. Phys. Chem. A* **2017**, *121* (14), 2748–2759.

(37) Candian, A.; Bouwman, J.; Hemberger, P.; Bodi, A.; Tielens, A. G. G. M. Dissociative ionisation of adamantane: A combined theoretical and experimental study. *Phys. Chem. Chem. Phys.* **2018**, *20*, 5399–5406.

(38) Bodi, A.; Hemberger, P. Low-energy photoelectron spectrum and dissociative photoionization of the smallest amides: Formamide and acetamide. *J. Phys. Chem. A* **2019**, *123* (1), 272–283.

(39) Wu, X.; Zhou, X.; Hemberger, P.; Bodi, A. A guinea pig for conformer selectivity and mechanistic insights into dissociative ionization by photoelectron photoion coincidence: Fluorocyclohexane. *Phys. Chem. Chem. Phys.* **2020**, *22* (4), 2351–2360.

(40) Baer, T.; Tuckett, R. P. Advances in threshold photoelectron spectroscopy (TPES) and threshold photoelectron photoion coincidence (TPEPICO). *Phys. Chem. Chem. Phys.* **2017**, *19* (15), 9698–9723.

(41) Wu, X.; Tang, X.; Zhou, X.; Liu, S. Dissociation dynamics of energy-selected ions using threshold photoelectron-photoion coincidence velocity imaging. *Chin. J. Chem. Phys.* **2019**, *32* (1), 11–22.

(42) Bodi, A.; Baer, T.; Wells, N. K.; Fakhoury, D.; Klecyngier, D.; Kercher, J. P. Controlling tunnelling in methane loss from acetone ions by deuteration. *Phys. Chem. Chem. Phys.* **2015**, *17* (43), 28505–28509.

(43) Bodi, A.; Hemberger, P. Low-energy photoelectron spectrum and dissociative photoionization of the smallest amides: Formamide and acetamide. *J. Phys. Chem. A* **2019**, *123* (1), 272–283.

- (44) Steglich, M.; Custodis, V. B.; Trevitt, A. J.; daSilva, G.; Bodi, A.; Hemberger, P. Photoelectron spectrum and energetics of the meta-xylylene diradical. *J. Am. Chem. Soc.* **2017**, *139* (41), 14348–14351.
- (45) Voronova, K.; Ervin, K. M.; Torma, K. G.; Hemberger, P.; Bodi, A.; Gerber, T.; Osborn, D. L.; Sztáray, B. I. Radical thermometers, thermochemistry, and photoelectron spectra: A photoelectron photoion coincidence spectroscopy study of the methyl peroxy radical. *J. Phys. Chem. Lett.* **2018**, *9* (3), 534–539.
- (46) Lesniak, L.; Salas, J.; Burner, J.; Diedhiou, M.; Burgos Paci, M. A.; Bodi, A.; Mayer, P. M. Trifluoroacetic acid and trifluoroacetic anhydride radical cations dissociate near the ionization limit. *J. Phys. Chem. A* **2019**, *123* (29), 6313–6318.
- (47) Bauer, C. A.; Grimme, S. How to compute electron ionization mass spectra from first principles. *J. Phys. Chem. A* **2016**, *120* (21), 3755–3766.
- (48) Johnson, M.; Bodi, A.; Schulz, L.; Gerber, T. Vacuum ultraviolet beamline at the swiss light source for chemical dynamics studies. *Nucl. Instrum. Methods Phys. Res., Sect. A* **2009**, *610* (2), 597–603.
- (49) Sztáray, B.; Voronova, K.; Torma, K. G.; Covert, K. J.; Bodi, A.; Hemberger, P.; Gerber, T.; Osborn, D. L. CRF-PEPICO: Double velocity map imaging photoelectron photoion coincidence spectroscopy for reaction kinetics studies. *J. Chem. Phys.* **2017**, *147* (1), 013944.
- (50) Kramida, A.; Ralchenko, Y.; Reader, J.; NIST ASD Team. *NIST Atomic Spectra Database*, version 5.8, [online]; National Institute of Standards and Technology: Gaithersburg, MD, 2020; <https://physics.nist.gov/asd> (accessed March 7, 2021).
- (51) Bodi, A.; Sztáray, B.; Baer, T.; Johnson, M.; Gerber, T. Data acquisition schemes for continuous two-particle time-of-flight coincidence experiments. *Rev. Sci. Instrum.* **2007**, *78* (8), 084102.
- (52) Sztáray, B.; Baer, T. Suppression of hot electrons in threshold photoelectron photoion coincidence spectroscopy using velocity focusing optics. *Rev. Sci. Instrum.* **2003**, *74* (8), 3763–3768.
- (53) West, B.; Joblin, C.; Blanchet, V.; Bodi, A.; Sztáray, B. I.; Mayer, P. M. On the dissociation of the naphthalene radical cation: New iPEPICO and tandem mass spectrometry results. *J. Phys. Chem. A* **2012**, *116* (45), 10999–11007.
- (54) Weidner, P.; Voronova, K.; Bodi, A.; Sztáray, B. Dissociative photoionization of 1,3-dioxolane: We need six channels to fit the elephant. *J. Mass Spectrom.* **2020**, *55*, e4522.
- (55) Voronova, K.; Easter, C. M. M.; Covert, K. J.; Bodi, A.; Hemberger, P.; Sztáray, B. Dissociative photoionization of diethyl ether. *J. Phys. Chem. A* **2015**, *119*, 10654–10663.
- (56) Rice, O. K.; Ramsperger, H. C. Theories of unimolecular gas reactions at low pressures. *J. Am. Chem. Soc.* **1927**, *49* (7), 1617–1629.
- (57) Rice, O. K.; Ramsperger, H. C. Theories of unimolecular gas reactions at low pressures. *J. Am. Chem. Soc.* **1928**, *50* (3), 617–620.
- (58) Marcus, R. A.; Rice, O. K. The kinetics of the recombination of methyl radicals and iodine atoms. *J. Phys. Chem.* **1951**, *55* (6), 894–908.
- (59) Curtiss, L. A.; Redfern, P. C.; Raghavachari, K. Gaussian-4 theory. *J. Chem. Phys.* **2007**, *126* (8), 084108.
- (60) Frisch, M. J.; Trucks, G. W.; Schlegel, H. B.; Scuseria, G. E.; Robb, M. A.; Cheeseman, J. R.; Scalmani, G.; Barone, V.; Mennucci, B.; Petersson, G. A.; et al. *Gaussian 16*, revision A.03; Gaussian, Inc.: Wallingford, CT, 2016.
- (61) Montgomery, J. A.; Frisch, M. J.; Ochterski, J. W.; Petersson, G. A. A complete basis set model chemistry. VII. Use of the minimum population localization method. *J. Chem. Phys.* **2000**, *112* (15), 6532–6542.
- (62) Martin, J. M. L.; de Oliveira, G. Towards standard methods for benchmark quality ab initio thermochemistry - W1 and W2 theory. *J. Chem. Phys.* **1999**, *111* (5), 1843–1856.
- (63) Stanton, J. F.; Gauss, J. Analytic energy derivatives for ionized states described by the equation-of-motion coupled cluster method. *J. Chem. Phys.* **1994**, *101* (10), 8938–8944.
- (64) Shao, Y.; Molnar, L. F.; Jung, Y.; Kussmann, J.; Ochsenfeld, C.; Brown, S. T.; Gilbert, A. T.; Slipchenko, L. V.; Levchenko, S. V.; O'Neill, D. P. Advances in methods and algorithms in a modern quantum chemistry program package. *Phys. Chem. Chem. Phys.* **2006**, *8* (27), 3172–3191.
- (65) Wu, X.; Zhou, X.; Hemberger, P.; Bodi, A. The ionization energy of the vinyl radical: A mexican standoff with a happy ending. *Phys. Chem. Chem. Phys.* **2019**, *21* (40), 22238–22247.
- (66) Bodi, A.; Shuman, N. S.; Baer, T. On the ionization and dissociative photoionization of iodomethane: A definitive experimental enthalpy of formation of CH₃I. *Phys. Chem. Chem. Phys.* **2009**, *11* (46), 11013–11021.
- (67) Bodi, A.; Brannock, M. D.; Sztáray, B.; Baer, T. Tunneling in H loss from energy selected ethanol ions. *Phys. Chem. Chem. Phys.* **2012**, *14* (46), 16047–16054.
- (68) Torma, K. G.; Voronova, K.; Sztáray, B.; Bodi, A. Dissociative photoionization of the C₇H₈ isomers cycloheptatriene and toluene: Looking at two sides of the same coin simultaneously. *J. Phys. Chem. A* **2019**, *123* (16), 3454–3463.
- (69) Torma, K. G.; Voronova, K.; Ray, A. W.; Bodi, A.; Sztáray, B. What a little branching can do—dissociative photoionization of two butanol isomers. *Int. J. Mass Spectrom.* **2020**, *453*, 116341.
- (70) Covert, K. J.; Bodi, A.; Torma, K. G.; Voronova, K.; Baer, T.; Sztáray, B. To roam or not to roam, that is the question for the methyl group in isopropanol cations. *Int. J. Mass Spectrom.* **2021**, *459*, 116469.
- (71) Hornung, B.; Bodi, A.; Pongor, C. I.; Gengeliczki, Z.; Baer, T.; Sztáray, B. Dissociative photoionization of X(CH₃)₃ (X = N, P, As, Sb, Bi): Mechanism, trends, and accurate energetics. *J. Phys. Chem. A* **2009**, *113* (28), 8091–8098.
- (72) Hoener, M.; Bodi, A.; Hemberger, P.; Endres, T.; Kasper, T. Threshold photoionization shows no sign of nitril hydride in methane oxidation with nitric oxide. *Phys. Chem. Chem. Phys.* **2021**, *23* (2), 1265–1272.
- (73) Joalland, B.; Shi, Y.; Kamasah, A.; Suits, A. G.; Mebel, A. M. Roaming dynamics in radical addition–elimination reactions. *Nat. Commun.* **2014**, *5* (1), 4064.
- (74) Gerlach, M.; Bodi, A.; Hemberger, P. Metamorphic meta isomer: Carbon dioxide and ketenes are formed via retro-diels–alder reactions in the decomposition of meta-benzenediol. *Phys. Chem. Chem. Phys.* **2019**, *21* (35), 19480–19487.
- (75) Linstrom, P. J.; Mallard, W. G., Eds.; *NIST Chemistry Webbook, NIST Standard Reference Database Number 69*; National Institute of Standards and Technology: Gaithersburg, MD; <http://webbook.nist.gov> (accessed October 1, 2020).
- (76) Chen, Y.; Yu, T.; Wu, X.; Zhou, X.; Liu, S.; Liu, F.; Dai, X. C–F and C–H bond cleavage mechanisms of trifluoromethane ion in low-lying electronic states: Threshold photoelectron-photoion coincidence imaging and theoretical investigations. *Phys. Chem. Chem. Phys.* **2020**, *22* (24), 13808–13817.
- (77) Wu, X.; Yu, T.; Chen, Y.; Zhou, X.; Liu, S.; Dai, X.; Liu, F.; Sheng, L. Dissociative photoionization of CF₃Cl via the C²E and D²E states: Competition of the C–F and C–Cl bond cleavages. *Phys. Chem. Chem. Phys.* **2019**, *21* (9), 4998–5005.
- (78) Bodi, A.; Hemberger, P.; Tuckett, R. P. Coincident velocity map image reconstruction illustrated by the single-photon valence photoionisation of CF₃SF₅. *Phys. Chem. Chem. Phys.* **2017**, *19* (44), 30173–30180.
- (79) Wheeler, S. E.; Houk, K. N.; Schleyer, P. v. R.; Allen, W. D. A hierarchy of homodesmotic reactions for thermochemistry. *J. Am. Chem. Soc.* **2009**, *131* (7), 2547–2560.
- (80) Dorofeeva, O. V.; Osina, E. L. Performance of DFT, MP2, and composite ab initio methods for the prediction of enthalpies of formations of chon compounds using isodesmic reactions. *Comput. Theor. Chem.* **2017**, *1106*, 28–35.
- (81) Lebedeva, N.; Raydnenko, V.; Gutner, N.; Kiseleva, N. Enthalpies of formation for polysubstituted benzenes. *Thermodyn. Organ. Soedin.* **1976**, *5*, 12–6 (in Russian).

(82) Maksimuk, Y.; Ponomarev, D.; Sushkova, A.; Krouk, V.; Vasarenko, I.; Antonava, Z. Standard molar enthalpy of formation of vanillin. *J. Therm. Anal. Calorim.* **2018**, *131* (2), 1721–1733.

(83) Almeida, A. R.R.P.; Freitas, V. L.S.; Campos, J. I.S.; Ribeiro da Silva, M. D. M. C.; Monte, M. J.S. Volatility and thermodynamic stability of vanillin. *J. Chem. Thermodyn.* **2019**, *128*, 45–54.

(84) Ruscic, B.; Bross, D. H. Active thermochemical tables (ATcT) values based on version 1.122p of the thermochemical network (2020). <https://atct.anl.gov/>, (accessed November 1, 2020).

(85) Pedley, J. B. *Thermochemical data and Structures of Organic Compounds*; CRC Press: Thermodynamics Research Center: College Station, TX, 1994; Vol. 1.

(86) Simoes, R. G.; Agapito, F.; Diogo, H. P.; da Piedade, M. E. M. Enthalpy of formation of anisole: Implications for the controversy on the O–H bond dissociation enthalpy in phenol. *J. Phys. Chem. A* **2014**, *118* (46), 11026–11032.

(87) Mulder, P.; Korth, H.-G.; Pratt, D. A.; DiLabio, G. A.; Valgimigli, L.; Pedulli, G.; Ingold, K. Critical re-evaluation of the o–h bond dissociation enthalpy in phenol. *J. Phys. Chem. A* **2005**, *109* (11), 2647–2655.

(88) Wu, X.; Zhou, X.; Hemberger, P.; Bodi, A. Dissociative photoionization of chloro-, bromo-, and iodocyclohexane: Thermochemistry and the weak C–Br bond in the cation. *J. Phys. Chem. A* **2021**, *125* (2), 646–656.

(89) Allen, W. D.; Bodi, A.; Szalay, V.; Császár, A. G. Adiabatic approximations to internal rotation. *J. Chem. Phys.* **2006**, *124* (22), 224310.

(90) Pitzer, K. S.; Gwinn, W. D. Energy levels and thermodynamic functions for molecules with internal rotation i. Rigid frame with attached tops. *J. Chem. Phys.* **1942**, *10* (7), 428–440.

(91) McClurg, R. B. Comment on: “The hindered rotor density-of-states interpolation function” [*J. Chem. Phys.* 106, 6675 (1997)] and “the hindered rotor density-of-states” [*J. Chem. Phys.* 108, 2314 (1998)]. *J. Chem. Phys.* **1999**, *111* (15), 7163–7164.

(92) Borkar, S.; Sztáray, B.; Bodi, A. Dissociative photoionization mechanism of methanol isotopologues (CH_3OH , CD_3OH , CH_3OD and CD_3OD) by iPEPICO: Energetics, statistical and non-statistical kinetics and isotope effects. *Phys. Chem. Chem. Phys.* **2011**, *13* (28), 13009–13020.

(93) Varfolomeev, M. A.; Abaidullina, D. I.; Solomonov, B. N.; Verevkin, S. P.; Emel'yanenko, V. N. Pairwise substitution effects, inter- and intramolecular hydrogen bonds in methoxyphenols and dimethoxybenzenes. Thermochemistry, calorimetry, and first-principles calculations. *J. Phys. Chem. B* **2010**, *114* (49), 16503–16516.

(94) Matos, M. A. R.; Miranda, M. S.; Morais, V. M. Thermochemical study of the methoxy- and dimethoxyphenol isomers. *J. Chem. Eng. Data* **2003**, *48* (3), 669–679.

(95) Bernardes, C. E.; Minas da Piedade, M. E. Energetics of the O–H bond and of intramolecular hydrogen bonding in $\text{HOC}_6\text{H}_4\text{C}(\text{O})\text{Y}$ ($\text{Y} = \text{H}$, CH_3 , $\text{CH}_2\text{CH}=\text{CH}_2$, $\text{C}\equiv\text{CH}$, CH_2F , NH_2 , NHCH_3 , NO_2 , OH , OCH_3 , OCN , CN , F , Cl , SH , and SCH_3) compounds. *J. Phys. Chem. A* **2008**, *112* (40), 10029–10039.

(96) Ribeiro da Silva, M. D. M. C.; Araujo, N. R.M. Thermochemical studies on salicylaldehyde and salicylamide. *J. Chem. Thermodyn.* **2007**, *39* (10), 1372–1376.

(97) Ribeiro da Silva, M. D. M. C.; Goncalves, M. V.; Monte, M. J.S. Thermodynamic study on hydroxybenzaldehyde derivatives: 3- and 4-hydroxybenzaldehyde isomers and 3,5-di-tert-butyl-2-hydroxybenzaldehyde. *J. Chem. Thermodyn.* **2010**, *42* (4), 472–477.

(98) Serpinskiĭ, V.; Voitkevich, S.; Lyuboshits, N. Y. Determination of the vapor pressures of several fragrant substances. *Zh. Fiz. Khim.* **1953**, *27*, 1032–1038 (in Russian).